

Goodarzi M, Rouainia M, Aplin AC, Cubillas P, de Block M.

[Predicting the elastic response of organic-rich shale using nanoscale measurements and homogenisation methods.](#)

Geophysical Prospecting (2017)

DOI: <https://doi.org/10.1111/1365-2478.12475>

Copyright:

This is the peer reviewed version of the following article, which has been published in final form at <https://doi.org/10.1111/1365-2478.12475>. This article may be used for non-commercial purposes in accordance with Wiley Terms and Conditions for Self-Archiving.

Date deposited:

23/10/2016

Embargo release date:

24 January 2018

Predicting the elastic response of organic-rich shale using nanoscale measurements and homogenisation methods

M. Goodarzi¹, M. Rouainia¹, A.C. Aplin², P. Cubillas² and M. de Block³

¹*School of Civil Engineering and Geosciences, Newcastle University, Newcastle NE1 7RU, UK*

²*Department of Earth Sciences, Durham University, DH1 3LE, UK*

³*SGS Horizon B.V., Stationsplein 6, Voorburg, 2275 AZ, Netherlands*

Abstract

Determination of the mechanical response of shales through experimental procedures is a practical challenge due to their heterogeneity and the practical difficulties of retrieving good quality core samples. Here, we investigate the possibility of using multi-scale homogenisation techniques to predict the macroscopic mechanical response of shales, based on quantitative mineralogical descriptions. We use the novel PeakForce Quantitative Nanomechanical Mapping (QNM[®]) technique to generate high resolution mechanical images of shales, allowing the response of porous clay, organic matter and mineral inclusions to be measured at the nanoscale. These observations support some of the assumptions previously made in the use of homogenisation methods to estimate the elastic properties of shale, and also earlier estimates of the mechanical properties of organic matter. We evaluate the applicability of homogenisation techniques against measured elastic responses of organic-rich shales, partly from published data and also from new indentation tests carried out in this work. Comparison of experimental values of the elastic constants of shale samples with those predicted by homogenisation methods showed that almost all predictions were within the standard deviation of experimental data. This suggests that the homogenisation approach is a useful way of estimating the elastic and mechanical properties of shales, in situations where conventional rock mechanics test data cannot be measured.

Key words: Anisotropy, Elastics, Imaging, Modelling, Rock physics.

1 Introduction

Shale, or mudstone, is the most common sedimentary rock: a heterogeneous, multi-mineralic natural composite consisting of clay mineral aggregates, organic matter and variable quantities of minerals such as quartz, calcite and feldspar. Shale plays a key role as a top seal to many petroleum reservoirs and CO₂ storage sites, as a low permeability barrier for nuclear waste and as an unconventional petroleum reservoir. In all these contexts, and as a material which needs to be effectively drilled when exploring for petroleum, the mechanical properties of shale are critical but quite poorly constrained. For example, there are relatively few laboratory-based studies where mechanical data have been measured on shales which have been well-characterised in terms of mineralogy and microstructure. In part, this is due to the chemical and mechanical instability of shales, which means that it is challenging and expensive to retrieve good quality core samples for undertaking conventional rock mechanics experiments (Kumar, Sondergeld and Rai 2012). Furthermore, because shales are heterogeneous on many scales (e.g. Aplin and Macquaker 2011), it is not straightforward to relate macroscopic experimental measurements to microscopic structural data.

Recently, micromechanical indentation tests have been performed on shales (Zeszotarski et al. 2004; Ulm and Abousleiman 2006). Although this technique is fast and can be performed on commonly available drill cuttings, the data have limited scope as they cannot fully characterize the mechanical response of the material. However, indentation is useful for comparing the mechanical response of different materials. Another approach is to adopt micro-mechanical models that have been widely used in the field of composite engineering (Klusemann, Bohm and Svendsen 2012; Mortazavi et al. 2013). In these methods, the macroscale mechanical behaviour of a composite is determined from the mechanical response of each constituent along with their interaction with each other. This modelling approach is in principle well suited to shale, the mechanical properties of which are likely to depend on the porosity, the volume fraction of solid mineral inclusions and the amount of organic matter (Sayers 2013a).

In their pioneering work on the micro-mechanical modelling of the anisotropic elastic response of shales, Hornby, Schwartz and Hudson (1994) assumed an isotropic intrinsic response for the solid unit of clay into which macroscopic anisotropy was introduced through platelet-shaped clay particles, their orientation and interparticle nanopores. Silt inclusions were then added as spherical isolated grains. Subsequent work modified this approach to provide an improved description of the elastic response of shales, including the incorporation of organic matter into the shale microstructure model (Sayers 1994; Jakobson, Hudson and Johansen 2003; Ortega, Ulm and Abousleiman 2007; Zhu et al. 2012; Vasin et al. 2013; Sayers 2013a; Qin, Han and Zhao 2014). The main difference between these studies relates to the homogenisation strategies used to upscale the shale matrix (containing solid clay, kerogen and fluid phases), as well as the properties of the solid clay and kerogen. For example, Zhu et al. (2012) and Qin et al. (2014) considered kerogen as elliptical inclusions embedded into the shale microstructure. Guo, Li and Liu (2014) followed the same approach as Hornby et al. (1994), combining clay particles with kerogen and adding pores as spherical, isolated inclusions. In contrast, Vernik and Landis (1996) considered kerogen as an isotropic background matrix for the shale, which causes a reduction of the elastic constants. However, Sayers (2013b) showed that a model in

43 which the matrix is described as a transversely isotropic (TI) kerogen and the shale as inclusion
44 provides a better prediction of the elastic stiffness.

45 Clearly, several quite different modelling approaches have been proposed to explain exper-
46 imental observations, further highlighting the complexity of shales. In some studies (e.g. Wu
47 et al. 2012; Zu et al. 2013), multiple micro-structural features, such as the amount of pores
48 and their aspect ratios in both clay and kerogen, kerogen particle aspect ratio, cracks, etc., were
49 considered numerically. However, these features could not be directly measured and need to
50 be calibrated. Although it is computationally possible to add any level of detail to a model, it
51 should be noted that different combinations of these micro-structural features can produce the
52 same overall mechanical response. Consequently, it is still difficult to be sure of the micro-
53 structural factors which contribute most to the overall anisotropic response of shales (Bayuk,
54 Ammerman and Chesnokov 2008).

55 Two key issues need to be resolved in order to successfully implement multi-scale modelling
56 approaches. Firstly, the mechanical properties of the elementary building blocks of shales must
57 be known. Whilst the mechanical properties of phases such as calcite and quartz are reason-
58 ably well constrained, those of the solid unit of the porous clay and of organic matter are less
59 well known. The second issue is the selection of an appropriate homogenisation strategy with
60 which to account for the shale micro-structure and capture its behaviour at a macroscopic scale.
61 With these two issues in mind, the objective of the present study is to assess the capabilities of
62 multi-scale homogenisation methods to predict the elastic mechanical response of organic-rich
63 shales using experimental measurements from nano to macro scales. In the first section, the
64 adopted homogenisation formulation is discussed, along with its capabilities and limitations.
65 Having described the input data required for this approach, we then use the recently developed
66 Atomic Force Microscopy (AFM) technique, PeakForce QNM[®], to investigate the nanoscale
67 mechanical response of the individual phases, since these are fundamental inputs to the ho-
68 mogenisation schemes. Published mechanical measurements using Ultra-sonic Pulse Velocity
69 (UPV) test on core samples are then used to evaluate the predictions of the homogenisation
70 method. Finally, indentation moduli measured parallel and perpendicular to bedding in several
71 characterised organic-rich shale samples are used to further test the multi-scale homogenisation
72 formulation for predicting the shale elastic response.

73 **2 Multi-scale homogenisation formulation**

74 Here, shale is assumed to be a composite formed by a porous matrix in which solid mineral
75 grains/inclusions are randomly distributed (Figure 1). As a result, two levels of homogenisation
76 need to be implemented for shales. At the first level, the properties of the shale matrix are
77 upscaled using the porosity and properties of the solid unit of clay and organic matter. At the
78 second level, the macroscale shale behaviour is obtained using the homogenised properties of
79 the porous matrix from the previous level, plus the volume fractions and the properties of the
80 different silt inclusions.

81 Goodarzi, Rouainia and Aplin (2016) studied the performance and accuracy of various for-
82 mulations using numerical analyses. Different microstructures for the porous clay and also
83 the matrix-inclusion morphology were considered. Based on these microstructures, numeri-

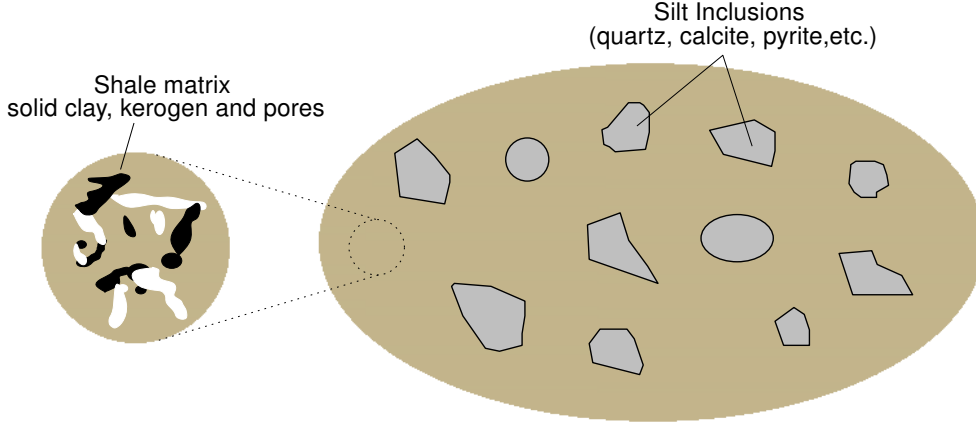


Figure 1: Two levels of shale micro-structure: shale matrix and the matrix-inclusion morphology.

84 cal models were generated and the macroscale elastic responses were obtained using boundary
 85 conditions which replicate uniaxial and hydrostatic compression tests. They conducted numer-
 86 ical simulations of a porous composite in which the shale microstructure ranged from a simple
 87 system of one inclusion/void embedded in a matrix, to complex, random microstructures devel-
 88 oped from SEM images. They concluded that although the pores are considered as spherical
 89 isolated voids in the Self-Consistent Scheme (SCS) (Hill 1965) calculation, the predicted re-
 90 sults are in good agreement with porous media with connected or random pore networks. The
 91 SCS model also makes a linear prediction for stiffness versus porosity up to a porosity of 0.5,
 92 in good agreement with nanoindentation results on porous clay (Ulm and Abousleiman 2006;
 93 Bobko and Ulm 2008). Further, Goodarzi et al. (2016) also found that for matrix-inclusion
 94 morphologies containing up to 40% of inclusion, the homogenised Young's modulus is better
 95 predicted using SCS, whilst the Mori-Tanaka model (MT) (Mori and Tanaka 1973) provides
 96 better results for the homogenised bulk modulus. For volume fractions above 40%, the predic-
 97 tion error for these schemes increases gradually. Overall, these results suggest that SCS can be
 98 adopted for the first level of homogenisation.

99 Several formulations have been proposed to upscale the elastic response of a composite,
 100 each making certain assumptions about the geometry of, and interaction between the various
 101 constituents. A key challenge is to select a formulation which best captures the macroscopic
 102 behaviour.

103 The closed-form solution for the SCS is obtained by assuming that a single inclusion is em-
 104 bedded in a homogenised composite. Within this formulation, no single phase is considered to
 105 act as the matrix and all the phases are given equal importance. The derived nonlinear equation
 106 requires an iterative procedure to be solved for the homogenised elastic stiffness tensor and is
 107 given as follows:

$$\mathbb{C}_{\text{hom}} = \sum_{r=1}^N f_r \mathbb{C}_r : [\mathbb{I} + \mathbb{P}_{\mathbb{I}_r}^{\text{hom}} : (\mathbb{C}_r - \mathbb{C}_{\text{hom}})]^{-1} \quad (1)$$

108 where \mathbb{C}_{hom} is the fourth order stiffness tensor for the composite, \mathbb{C}_r is the stiffness tensor and

109 f_r is the volume fraction of the phase r , N is the total number of phases, \mathbb{I} is the symmetric
 110 identity tensor, and $\mathbb{P}_{I_r}^{\text{hom}}$ is the Hill tensor which depends on the shape and the properties of
 111 the phase and the homogenised stiffness tensor of the composite. The stiffness tensor for a
 112 transversely isotropic material is described in terms of five independent components which can
 113 be written in the matrix notation as:

$$C = \begin{bmatrix} C_{11} & C_{12} & C_{13} & 0 & 0 & 0 \\ C_{12} & C_{11} & C_{13} & 0 & 0 & 0 \\ C_{13} & C_{13} & C_{33} & 0 & 0 & 0 \\ 0 & 0 & 0 & 2C_{44} & 0 & 0 \\ 0 & 0 & 0 & 0 & 2C_{44} & 0 \\ 0 & 0 & 0 & 0 & 0 & 2C_{66} \end{bmatrix} \quad \text{with} \quad C_{66} = \frac{1}{2}(C_{11} - C_{12}) \quad (2)$$

114 The MT scheme, on the other hand, is based on the assumption that the inclusion is embed-
 115 ded in a layer of the matrix and an additional interaction term takes into account the effect of
 116 the adjacent inclusions. The final expression for MT scheme can be written as:

$$\mathbb{C}_{\text{hom}} = \sum_{r=1}^N f_r \mathbb{C}_r : [\mathbb{I} + \mathbb{P}_{I_r}^0 : (\mathbb{C}_r - \mathbb{C}_0)]^{-1} \left[\sum_{s=0}^N f_r [\mathbb{I} + \mathbb{P}_{I_s}^0 : (\mathbb{C}_s - \mathbb{C}_0)]^{-1} \right]^{-1} \quad (3)$$

117 where \mathbb{C}_0 is the stiffness tensor for the matrix phase, and $\mathbb{P}_{I_s}^0$ is the Hill tensor which here it
 118 depends on the shape and the properties of the phase r and the homogenised stiffness tensor
 119 of the matrix. Obtaining the Hill's tensor for the case of an anisotropic matrix is not trivial as
 120 it requires determination of Green's function, which is extremely complicated for transversely
 121 isotropic materials (Laws 1977). Laws (1977) derived an integral expression for Hill's tensor
 122 in this particular case which does not require knowledge of Green's function. For explicit for-
 123 mulae of Hill's tensor components for a spherical inclusion embedded in transversely isotropic
 124 matrices, readers are referred to Fritsch and Hellmich (2007). To the best of our knowledge,
 125 this is the only reference providing these expressions correctly.

126 3 Material properties

127 From equations (1) and (3), it can be seen that the volume fractions and the stiffness tensors of
 128 all constituents are required to allow the calculation of the homogenised elastic response of the
 129 composite. The volume fraction and mineralogy of clay and mineral inclusions can be estimated
 130 using X-ray diffraction, and the amount of organic matter measured by chemical analysis. A
 131 good estimation of the porosity, which can be measured in various ways, is also essential to the
 132 calculation of the clay matrix properties. The entire porosity of the sample is assumed to exist
 133 in the shale matrix, so that the porosity of the this matrix, ϕ_{matrix} , which is used in the first level
 134 of homogenisation, is calculated as:

$$\phi_{\text{matrix}} = \frac{\phi_{\text{shale}}}{1 - f_{\text{inc}}} \quad (4)$$

135 where ϕ_{shale} represents the shale porosity and f_{inc} is the total volume of non-clay minerals.
 136 For dry conditions, porosity is taken to be a constituent with zero stiffness. However, in fully
 137 saturated shale, the stiffness properties of water within pores (i.e. bulk stiffness $K = 2.2$ GPa
 138 and shear stiffness $G = 0$ GPa) needs to be considered (Hornby et al. 1994; Vasin et al. 2013).

139 Model implementation requires certain assumptions to be made about the properties of the
 140 different phases in shale. The shape and orientation of both inclusions and pores are generally
 141 considered to be important sources of the macroscopic anisotropic response of shales (Vasin et
 142 al. 2013). Nanoscale indentation tests performed on several shale samples with a different level
 143 of porosity in their clay matrices revealed that the solid part of the porous clay exhibits a sig-
 144 nificant, intrinsic, anisotropic elastic response which gradually reduces with increasing porosity
 145 (Ulm and Abousleiman 2006; Bobko and Ulm 2008). Ortega, Ulm and Abousleiman (2010)
 146 used a micro-mechanical approach to study the simultaneous effects of (a) anisotropy of the
 147 porous clay matrix, which was assumed to originate from solid clay particles, and (b) the shape
 148 and orientation of silt inclusions on the transversely isotropic elastic behaviour of bulk shale.
 149 They concluded that the possible contribution of the shape and orientation of silt inclusions on
 150 the macroscopic anisotropy of the shale is insignificant compared to the anisotropy of the clay
 151 matrix. This theoretical approach is also consistent with previous modelling and experimental
 152 studies in which an inverse correlation between silt inclusion content and anisotropy has been
 153 demonstrated (e.g. Bayuk et al. 2008; Guo et al. 2014).

154 In addition, incorporating the effect of inclusion shape into multi-scale homogenisation re-
 155 quires additional experimental data which makes this approach inefficient from a practical point
 156 of view.

157 Here, inclusions such as quartz, calcite, pyrite, etc, are considered to be spherical and to have
 158 isotropic elastic moduli which can be found in the literature (Table 1). The solid unit of porous
 159 clay, on the other hand, is assumed to be anisotropic; furthermore, its properties cannot be
 160 directly measured using conventional rock mechanics tests. Ortega et al. (2007) assumed that
 161 the overall anisotropy of shale originates from a solid unit of clay with universal mechanical
 162 properties. The elastic constants of the solid unit of clay as a transversely isotropic material
 163 were estimated by back-analysing from UPV measurements on shale core samples. It should
 164 be noted that this solid phase could be an agglomerate of clay particles. Table 2 provides the
 165 values obtained by Ortega et al. (2007).

Table 1: Properties of common minerals in shales (Bass 1995; Mavko, Mukerji and Dvorkin 2009; Whitaker et al. 2010).

Minerals	Elastic properties	
	E (GPa)	Poisson's ratio
Quartz	101	0.06
Calcite	95	0.28
Pyrite	265.4	0.18
Feldspar	73.7	0.26
Dolomite	118	0.29

Table 2: Solid clay properties (data from Ortega et al. 2007).

Elastic Constant	Value (GPa)
C_{11}	44.9
C_{33}	24.2
C_{13}	18.1
C_{66}	11.6
C_{44}	3.7
$C_{12}=(C_{11} - 2C_{66})$	21.7

166 The assumption that only one set of elastic constants can be used for the solid unit of clay
167 (e.g. Ortega et al. 2007; Table 2), regardless of mineralogy, is debatable and so it is of interest
168 to compare Ortega et al.'s values with those used in previous studies. Hornby et al. (1994) back-
169 calculated the solid clays elastic constants from an experimental data set on clay-fluid composite
170 as $K = 22.9$ GPa and $G = 10.6$ GPa, assuming isotropic conditions. Similar values of $K = 25$
171 GPa and $G = 9$ GPa are provided in Mavko et al. (2009). These values have been adopted
172 in several micromechanical models of shales with satisfactory results, regardless of the clay
173 mineralogy (Jakobsen et al. 2003; Draege, Jakobsen and Johansen 2006; Wu et al. 2012; Sayers
174 2013a; Qin et al. 2014; Guo et al. 2014). Converting the anisotropic properties in Table 2 using
175 the Voigt average (Antonangeli et al. 2005) to its equivalent isotropic form results in comparable
176 values of $K = 23.9$ GPa and $G = 6.7$ GPa. Considering these micromechanical models and also
177 nanoindentation test data (Ulm and Abousleiman 2006), the assumption of constant properties
178 for the elementary building block of porous clay can be adopted confidently. Additionally, it
179 should be noted that the presented values are still much lower than the ones obtained for a single
180 clay particle (Wang, Wang and Cates 2001). Bobko and Ulm (2008) justified this difference by
181 assuming that the porous clay has a nano-granular microstructure. They concluded that the
182 mechanical response of porous clay might be mainly determined by chemical and mechanical
183 interactions in contacts between individual clay particles or clay agglomerates, rather than the
184 intrinsic mechanical response of a single clay particle.

185 Shale gas and oil reservoirs contain significant amounts of organic matter, which has a wide
186 range of measured elastic properties. Zeszotarski et al. (2004) performed nanoindentation tests
187 on kerogen in Woodford shale. An isotropic behaviour was observed and if Poisson's ratio is
188 assumed to be 0.3, then the Young's modulus is estimated to be 11.5 GPa. The same approach
189 was adopted by Kumar (2012) and Zargari et al. (2013), who generated values of less than 2 GPa
190 for highly porous kerogen. Vernik and Nur (1992) used the thin-layer composite concept and
191 back-analysed the mechanical properties of kerogen, concluding that kerogen is isotropic with
192 values of 8 GPa and 0.28 for the Young's modulus and the Poisson's ratio, respectively. Yan
193 and Han (2013) used effective medium theory and back-calculated the Young's modulus of 4.5,
194 6.42, 10.7 GPa for immature, mature and overmature organic matter, respectively. Eliyahu et al.
195 (2015) performed PeakForce QNM[®] tests with an atomic force microscope to make nanoscale
196 measurements of the Young's modulus of organic matter in a shale thin section. Results ranged
197 from 0-25 GPa with a modal value of 15 GPa. Due to the relative softness of organic matter,

198 the mechanical behaviour of shales may be significantly influenced by even small amounts
199 of organic matter (Vernik and Milovac 2011; Sayers 2013b). This can lead to difficulties in
200 implementing homogenisation techniques for these materials.

201 4 Nanoscale mechanical mapping of shales

202 Since shales are mainly formed of particles which range in size from smaller than 0.1 microns
203 to 100 microns, it follows that a high resolution technique is required to measure the mechanical
204 properties of individual particles or constituents in situ. Conventional small-scale mechanical
205 testing methods such as indentation can extract discontinuous data, but only at a resolution of at
206 least several microns. In contrast, the recently developed AFM technique known as PeakForce
207 QNM[®] is a non-destructive method which measures the elastic response of a material surface
208 with a resolution of a few nanometres. In this mode, an AFM probe is tapped over the surface
209 (using a sinusoidal signal) and the peak force applied on the surface is used as a feedback pa-
210 rameter to track the scanned surface (i.e. the peak force is continuously monitored and kept
211 constant during scanning). The mechanical response of the sample is extracted using the gener-
212 erated force-separation curve (one for every approach-withdraw cycle). The reduced Young's
213 modulus can be calculated by fitting the Derjaguin-Muller-Toporov (DMT) model for contact
214 mechanics on the curve obtained through the retracting stage of the tip movement (see Figure
215 2). According to this model the relationship between peak force (F_{pf}), adhesion force (F_{adh})
216 and the reduced Young's modulus, E^* , is as follows:

$$F_{pf} - F_{adh} = \frac{3}{4} E^* \sqrt{R(d - d_0)^3} \quad (5)$$

217 where R is the tip radius and $(d - d_0)$ is the sample deformation. The modulus obtained from
218 equation (5) can be related to the sample elastic response as:

$$E^* = \left(\frac{1 - \nu_s}{E_s} + \frac{1 - \nu_{tip}}{E_{tip}} \right)^{-1} \quad (6)$$

219 where E is the Young's modulus, ν is the Poisson's ratio and subscripts s and tip represent the
220 sample and tip, respectively.

221 In order to achieve reliable data several calibration procedures should be performed. First,
222 the effective tip radius is determined by probing a polycrystalline titanium standard sample.
223 Second, the deflection sensitivity of the cantilever is measured by pushing the tip against a
224 sapphire sample which serves as a surface with approximately infinite stiffness. The spring
225 constant of the tip is also required, and in this case was provided by the manufacturer (Bruker).
226 Finally, the calibrated system is evaluated against a standard pyrolytic graphite sample (HOPG-
227 12, Bruker) with a known mechanical response. For more information about the background
228 theory and calibration procedure of PeakForce QNM[®] readers are referred to Trtik, Kaufmann
229 and Volz (2012), Bruker's Application Note #141 and Bruker's Application Note #128.

230 After performing all the essential adjustments and calibration, PeakForce QNM[®] was im-
231 plemented to generate a high-resolution mechanical image of shale. For this purpose, an
232 organic-rich shale sample was characterised and two sections, parallel and perpendicular to

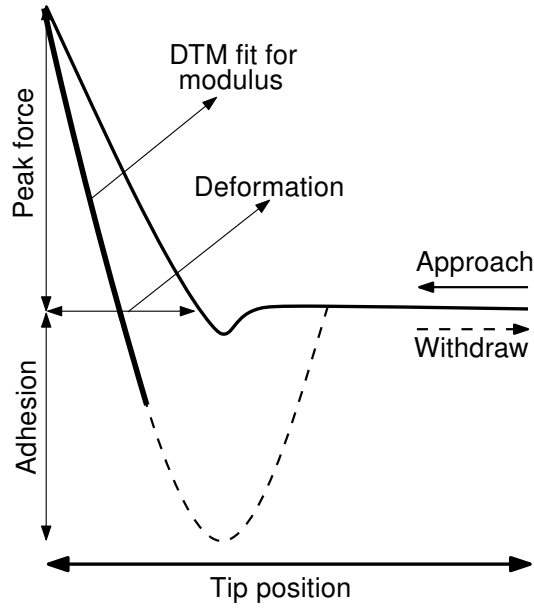


Figure 2: Schematic diagram of a generated force-separation curve for a single tapping of the PeakForce QNM[®] (Modified from Bruker's Application Note #128).

233 the bedding plane, were prepared (Table 3). Since a smooth surface is a key condition for
 234 good quality data in PeakForce QNM[®] and Indentation tests, the surfaces were hand polished
 235 and then polished using argon ion milling (Amirmajdi et al. 2009). Additionally, a suitable
 236 cantilever-tip assembly (with a relatively large stiffness $> 200 \text{ Nm}^{-1}$) is required to be able to
 237 measure the modulus on a shale, which contains stiff mineral grains ($E > 50 \text{ GPa}$) such as
 238 quartz. A diamond tip with a spring constant of 272 Nm^{-1} (DNISP; Bruker) was selected for
 239 this study. The tip was oscillated with 1 kHz frequency and the peak force was set to 50 –
 240 150 nN, as this provided the best results during the tests performed on the HOPG-12 standard.
 241 These settings generated 1-2 nm indentation depths on the sample.

Table 3: Characterisation of shale sample for the PeakForce QNM[®] test.

Mineralogy	Volume fraction (%)
Quartz	16.78
Calcite	0.23
Pyrite	2.91
Feldspar	0.59
Dolomite	0.00
Clay	65.97
Total organic carbon (TOC)	Weight (%)
	5.83
Porosity	9.45

242 4.1 Nano-mechanical image analysis

243 Figure 3 shows the elastic modulus map obtained on a $25 \times 25 \mu\text{m}^2$ area on the shale sample
244 perpendicular to the bedding direction (Figure 3d). Two types of grains with different, and
245 relatively high stiffness (> 50 GPa); and also areas with very low stiffness (< 30 GPa) can
246 be clearly recognised in this image. In order to better interpret the elastic modulus map, more
247 analyses including back-scattered electron (BSE) SEM imaging, energy dispersive spectroscopy
248 (EDS) chemical analysis and topographical data were also obtained from the same area (Figure
249 3). As part of the data analysis, it was initially assumed that the stiffer grains represent pyrite
250 (and were later identified as such from the EDS analysis (Figure 3b). An average value above
251 100 GPa was measured on pyrite grains which is lower than the reported values of 265 GPa
252 in the literature (see Table 1). The main reason for this deviation is that the reliable range of
253 measurable elastic modulus for the diamond tip is less than 80 GPa (Bruker's Application Note
254 #128). The mean value of the measured Young's modulus over the grains corresponding to
255 quartz in the EDS analysis (Figure 3b) is around 75 GPa, lower than the value reported in Table
256 1 but between the values reported by Elihayu et al. (2015), 63 ± 8 GPa, and Mavko et al.
257 (2009), 77 – 95 GPa. Again, it is difficult to be certain of this result because of the reliable
258 range of the tip.

259 Due to the stiffness difference of shale constituents, it is not possible to prepare a surface
260 as smooth as single phase materials such as the pyrolytic graphite sample which is used for the
261 calibration. Sample roughness may yield unreliable data. Comparing the topographical and the
262 mechanical maps (Figures 3c and 3d), it can be concluded that some soft areas are correlated
263 with abrupt deep areas on the sample. In fact, unlike the interpretation made by Eliyahu et al.
264 (2015), not all the soft regions can be attributed to organic matter and a careful comparison
265 between both the mechanical and topographical images is required to locate real soft phases
266 in the mechanical image. Such a comparison revealed the fact that the presence of the organic
267 matter phase in the shale composite is not similar to other inclusions such as quartz and pyrite.
268 This phase is intimately mixed within the porous clay rather than existing as isolated grains; this
269 is important when accounting for organic matter in the homogenisation techniques. Assuming
270 Poisson's ratio is 0.3 for this phase, the measured Young's moduli are less than 10 GPa with a
271 mean value of 6 GPa. Considering that the maturity of this sample is at a vitrinite reflectance of
272 0.5 – 0.6% (R_o), this result is consistent with the values of 6 – 9 GPa for immature kerogen
273 obtained by Kumar (2012).

274 As the macroscopic response of shales is highly anisotropic, it is of interest to look at
275 anisotropy at the nanoscale. Figure 4 shows the Young's modulus map of sections both par-
276 allel (E_1) and perpendicular (E_3) to the bedding direction. Two target areas were selected on
277 both images that contained porous clay and quartz grains. The measured data in these areas
278 were extracted and subjected to statistical analysis. Figure 5 illustrates the histogram and nor-
279 mal curve on the data and the mean values and standard deviations (SD) are provided in Table
280 4.

281 The mean values obtained on quartz grains are almost identical, producing an anisotropy
282 ratio (E_1/E_3) around 0.95. Although the measurements were taken from two different grains
283 with unknown orientations, this can be interpreted as an isotropic response for this phase. The

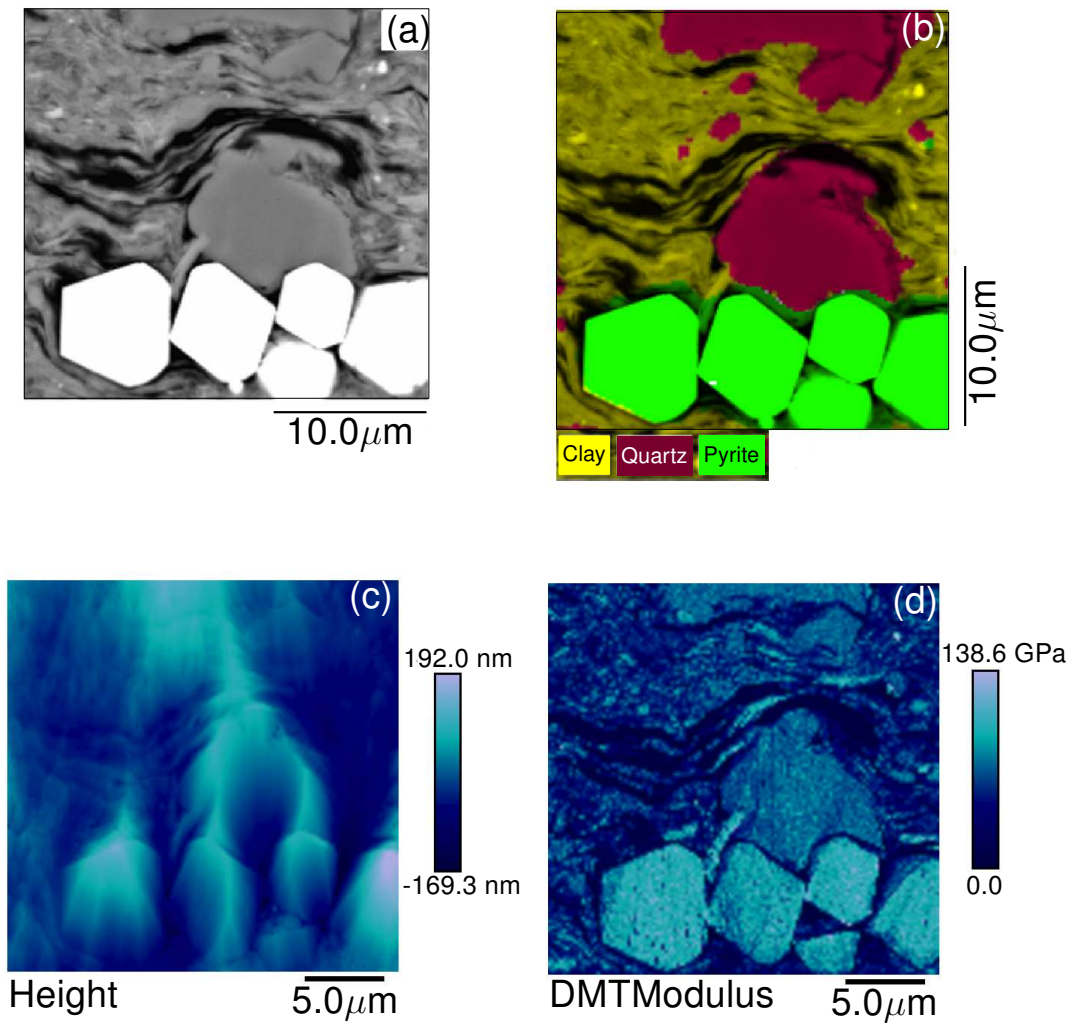


Figure 3: Different analyses on a target area perpendicular to the bedding direction. (a) SEM image using back scattered electron (BSE) imaging, (b) chemical analyses using energy dispersive spectrometry (EDS), (c) topography map taken during mechanical mapping and (d) Young's modulus map using PeakForce QNM[®].

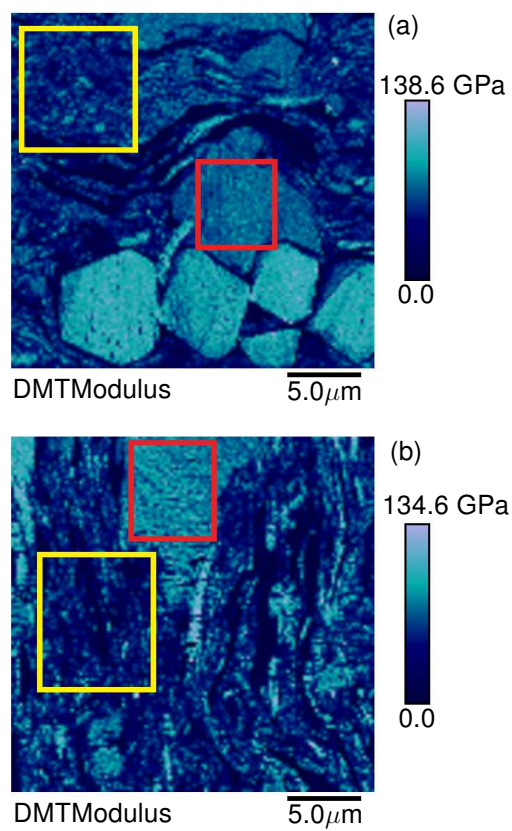


Figure 4: Yellow boxes are the target areas for porous clay and red boxes are the target areas for quartz on sections perpendicular (a) and parallel (b) to the bedding direction.

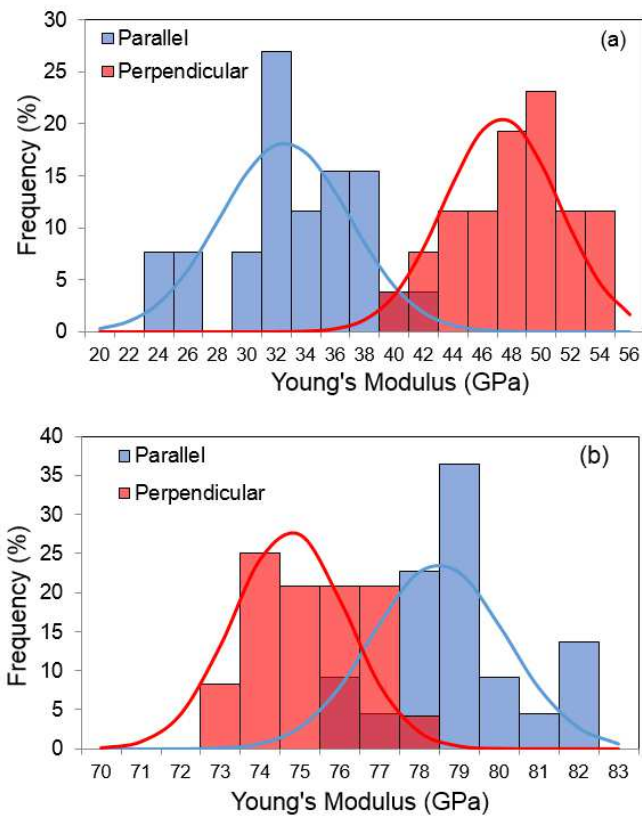


Figure 5: Histogram and normal curve of the measured Young's moduli on (a) porous clay and (b) quartz grain in both sections parallel and perpendicular to bedding direction.

284 observed, in situ elastic response of quartz grains within shale microstructure is different to
 285 measurements on large quartz crystals, which show noticeable anisotropy (Heyliger, Ledbetter
 286 and Kim 2003). Vasin et al. (2013) considered the full anisotropic elastic response of silt
 287 inclusions with random orientations in modelling shale anisotropy. However, since quartz grains
 288 in shales are randomly orientated with respect to the crystal structure, our observation supports
 289 the simple assumption made in Hornby et al. (1994) that accounts for mineral inclusions as a
 290 spherical, elastically isotropic phase.

291 The porous clay, on the other hand, shows significant anisotropy in these two sections with
 292 a ratio (E_1/E_3) around 1.45. An anisotropic ratio of 1.54 was obtained for a shale sample with
 293 almost the same porosity and inclusion volume fraction using UPV measurement on core sam-
 294 ples (Ulm and Abousleiman 2006). This comparison provides more support for the assumption,
 295 discussed in Section 3, about the origin of shale anisotropy. Additionally, the values obtained
 296 on the porous clay are higher than the properties assumed for a solid unit of porous clay here or
 297 the properties obtained by Hornby et al. (1994) (Table 2), but they are within the range of the
 298 properties reported for clay particles (Wang et al. 2001). Eliahayu et al. (2015) reported $29 \pm$
 299 1 GPa on the porous clay while they did not consider the direction of the section in their study.
 300 This value is very close to the measured data on the section perpendicular to bedding (see Table
 301 4). Further study is required to understand what type of micro-component of the porous clay
 302 was being touched by the tip.

Table 4: Predicted results (Pred) versus experimental measurements (Exp).

Sample No.	Clay packing density	Exp. M_1 (GPa)	Exp. M_3 (GPa)	Exp. M_1/M_3	Pred M_1 (GPa)	Pred. M_3 (GPa)	Pred. M_1/M_3	Error M_1 (%)	Error M_3 (%)
2	0.75	30.3	17.2	1.76	30.3	21.6	1.4	0.0	25
6	0.75	27.4	17	1.61	26.5	17.1	1.55	3.5	0.5
8	0.75	20.6	12.6	1.63	18.8	13.9	1.33	9	11.9
10	0.75	28.5	-	-	30.6	22.7	-	7.3	-

303 5 Implementation of multi-scale homogenisation techniques

304 The capabilities of homogenisation techniques in shales was investigated using numerical sim-
 305 ulations in which several virtual shale microstructures were generated and studied (Goodarzi et
 306 al. 2016). Good agreement was obtained between macroscopic elastic responses of the numer-
 307 ical rocks and the predicted values from the homogenisation methods.

308 However, it is clear that real composites, especially shales, are far more complex than the
 309 assumed numerical models and consequently it is important to validate the homogenisation
 310 techniques against several experimental data sets. Whilst UPV tests have been used to fully
 311 characterize the elastic response of shale samples, the experiment requires good quality core
 312 samples and is both technically difficult and time-consuming. Recently, indentation tests have
 313 been used to estimate the mechanical properties of shales. This test can be easily and efficiently

314 performed on shale cuttings and a good estimation on the anisotropic macroscopic elastic re-
315 sponse of shale can be obtained (Kumar et al. 2012; Ulm and Abousleiman 2006). Here,
316 published UPV results on well-characterised shales are used to evaluate the predictive capa-
317 bility of the homogenisation techniques. In addition, several organic-rich shale samples were
318 prepared, characterized and used to generate indentation data in order to extend the validation
319 data sets.

320 **5.1 Elastic response of shales porous clay**

321 The mechanical response of silt-grade mineral inclusions in shales are well known and possible
322 shape effects can be quantified using SEM or 3-D X-ray microtomographic imaging (Kanit-
323 panyacharoen et al. 2011; Vasin et al. 2013; Peng et al. 2015). However, neither the exact
324 microstructure of the porous clay, nor the properties of the solid unit of this composite, have
325 been fully evaluated. A complex network of pores including connected channels and isolated
326 pores at different scales have been experimentally observed in porous clay (e.g. Chalmers,
327 Bustin and Power 2012). Similarly, the organic matter occurs as a semi-continuous phase rather
328 than as isolated inclusions in the porous clay (see Figure 3). Consequently, the main challenge
329 in modelling the elastic behaviour of shales is the response of the matrix.

330 The main assumption in our approach is that the anisotropy originates from the solid clay,
331 having a transversely elastic response. The Self-Consistent Scheme is used to combine, without
332 any specific orientation distribution, the solid clay with the presence of pores and organic matter.
333 Aligned, platy clay minerals are not considered explicitly and the TI response compensates for
334 this effect. On the other hand, Hornby et al. (1994) assumed an isotropic response for the solid
335 clay and the anisotropy was subsequently generated by considering an oblate spheroid-shaped
336 clay particles and nanopores. The SCS was combined with a differential effective medium
337 model in order to satisfy the continuity of all the phases at any porosity level.

338 In order to clarify similarities and differences between the approach adopted in this paper
339 and the pioneering work of Hornby et al. (1994), all five elastic constants of a fully-saturated
340 porous clay are plotted as a function of porosity in Figure 6. Both approaches provide a similar
341 trend for the elastic constants as functions of fluid-filled porosity except for C_{44} , which shows
342 a drastic decrease with a small increase in porosity in the Hornby et al. (1994) formulation.
343 Additional differences can be partly attributed to the initial assumptions with regard to the
344 isotropy and anisotropy of the elastic properties of the solid unit of clay. It should be noted
345 that an increase or decrease in anisotropy can of course be introduced by considering elliptical
346 shapes with specific orientations for pores or organic matter in the SCS formulation. These two
347 modelling approaches give quite consistent results in reproducing the response of porous clay.

348 **5.2 UPV test data sets**

349 There are very few measurements of the mechanical behaviour of shales which are well char-
350 acterised in terms of both mineralogy and microstructure. Among these available data, those
351 which were not used by Ortega et al. (2007) to back-calculate the stiffness of the solid unit of
352 porous clay, were chosen for this study. Table 5 provides the mineralogical descriptions of these

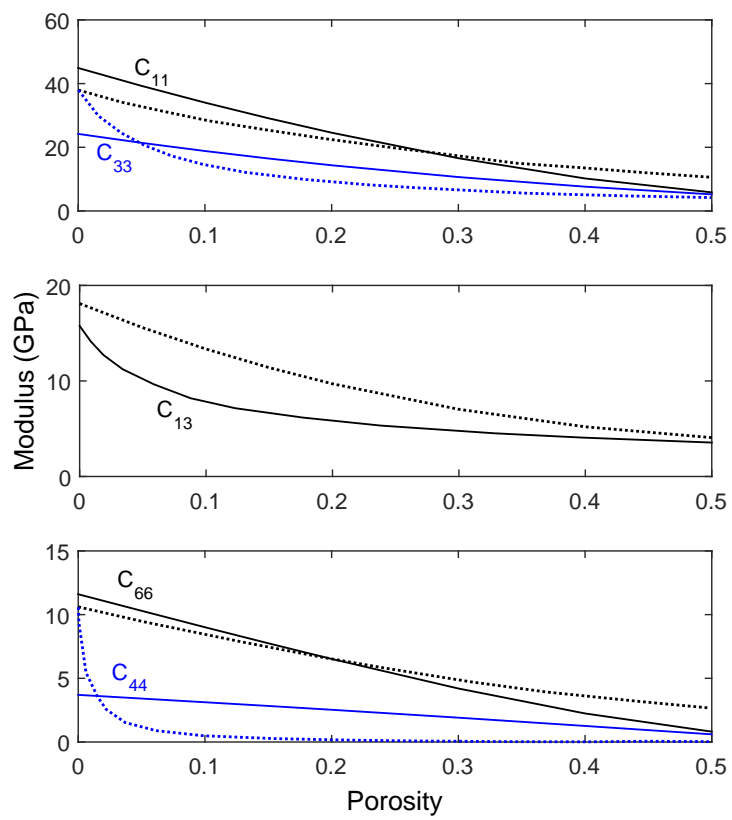


Figure 6: Saturated porous clay response versus porosity (solid lines are the results of this paper and dashed lines were extracted from Hornby et al. 1994).

353 samples. For the first two data sets, Kimmeridge and Jurassic shales, the elastic constants were
 354 measured in saturated conditions under different confining pressures. With increasing confining
 355 pressure, properties almost converged to constant values which we infer are due to the closure
 356 of microcracks. As cracks are not considered in our modelling, the values corresponding to
 357 the highest confining pressure, 80 MPa, were selected for comparison. For Woodford shales
 358 the natural water content of the samples was preserved but no information was provided on the
 359 confining pressure.

Table 5: Mineralogical data for the UPV data sets shale samples (extracted from Hornby 1998; Sierra et al. 2010)

Sample	Kimmeridge Shale	Jurassic Shale	Woodford-1 Shale	Woodford-2 Shale
Mineralogical Data	Volume Fraction (%)			
Quartz	30.5	31	-	-
Calcite	-	1	-	-
Pyrite	2.1	5	-	-
Feldspar	7.2	4	-	-
Dolomite	-	-	-	-
Clay	60.2	58	57.1	65.2
Sum of Non-Clay	39.8	42	42.9	34.8
Shale Porosity	2.5	10.5	16	15
Clay Porosity	4.15	18.1	28	23

360 The transversely isotropic elastic stiffness tensors were obtained for these four shales us-
 361 ing UPV tests conducted on core samples. The mineralogical data provided in Table 5 were
 362 used along with homogenisation methods to estimate the five elastic constants for each sample.
 363 The SCS was adopted for the first stage of homogenisation. Both MT and SCS formulations
 364 were implemented for the second stage, in which matrix-inclusion morphology is homogenised,
 365 in order to evaluate which strategy results in better predictions of macroscale mechanical be-
 366 haviour. In addition, the elastic properties of quartz were used to homogenise samples for
 367 which only the volume fraction of non-clay minerals are available, as this mineral is usually
 368 the most common non-clay mineral in shales. Figure 7 illustrates the predicted and the experi-
 369 mental results of the elastic constants of transversely isotropic shales using both SCS-SCS and
 370 SCS-MT strategies with bars showing the experimental standard deviation for each constant.
 371 The values of these constants, Thomsen's anisotropy parameters of $\varepsilon = (C_{11} - C_{33})/2C_{33}$ and
 372 $\gamma = (C_{66} - C_{44})/2C_{44}$ and their relative errors (%) are also given in Tables 6 and 7.

373 Comparing the relative errors between two up-scaling strategies revealed that there is no
 374 clear superiority for one strategy over the other one. This result can be justified due to the
 375 fact that each component of the stiffness tensor is a combination of two elastic constants, for
 376 example for an isotropic material $C_{11} = E(1 - \nu)/((1 + \nu)(1 - 2\nu))$. As it was highlighted
 377 in Section 2, numerical studies using SCS and MT schemes for predicting homogenised elastic
 378 response of matrix-inclusion morphology showed that each of this elastic constant can be better
 379 predicted with one of these schemes (Goodarzi et al. 2016). In fact, the error observed in

380 homogenised stiffness tensor components can be seen as the combined error of homogenised
381 elastic constants. It can be observed that both SCS-SCS and SCS-MT methods produce some
382 theoretical errors. However, in general, it can be concluded that SCS-SCS performed slightly
383 better, particularly in terms of capturing anisotropy.

Table 6: Experimental (Exp) and predicted (Pred) elastic constants for the UPV data sets samples using SCS-SCS.

Elastic constant	Kimmeridge Shale			Jurassic Shale			Woodford-2 Shale			Woodford-2 Shale		
	Exp.	Pred.	Error (%)	Exp.	Pred.	Error (%)	Exp.	Pred.	Error (%)	Exp.	Pred.	Error (%)
C_{11} (GPa)	56.2	56	0.35	46.1	45.3	1.73	25	35	40	28.3	34.6	22.2
C_{33} (GPa)	36.4	37	1.64	32.9	31.7	3.64	18.6	26	39.7	18.6	23.5	26.
C_{13} (GPa)	20.5	17.2	16.1	18.5	13.3	28.1	6.9	9.96	44.3	9.8	10.6	8.16
C_{66} (GPa)	18.9	18.2	3.70	14.3	15	4.9	7.8	11.8	51.2	9.3	11.1	19.3
C_{44} (GPa)	10.3	10.2	0.97	8.8	9.5	7.95	5.7	8.2	43.8	5.5	6.6	20
ε	0.27	0.26	5.5	0.2	0.21	6.9	0.17	0.17	0.0	0.26	0.23	9.4
γ	0.41	0.39	6.0	0.31	0.29	7.3	0.18	0.21	19	0.34	0.34	0.0

Table 7: Experimental (Exp) and predicted (Pred) elastic constants for the UPV data sets samples using SCS-SCS.

Elastic constant	Kimmeridge Shale			Jurassic Shale			Woodford-2 Shale			Woodford-2 Shale		
	Exp.	Pred.	Error (%)	Exp.	Pred.	Error (%)	Exp.	Pred.	Error (%)	Exp.	Pred.	Error (%)
C_{11} (GPa)	56.2	54.2	3.55	46.1	41.6	9.76	25	30.6	22.4	28.3	32.5	14.8
C_{33} (GPa)	36.4	33.5	8	32.9	26.4	19.7	18.6	20.6	10.7	18.6	20.7	11.2
C_{13} (GPa)	20.5	17.6	14.1	18.5	13.3	28.1	6.9	10.1	46.3	9.8	10.8	10.2
C_{66} (GPa)	18.9	17	10	14.3	13	9.1	7.8	9.5	21.7	9.3	9.9	6.45
C_{44} (GPa)	10.3	8.1	21.3	8.8	6.7	23.8	5.7	5.4	5.26	5.5	5.1	7.3
ε	0.27	0.31	0.13	0.2	0.28	43.5	0.17	0.24	41	0.26	0.28	9.3
γ	0.41	0.54	31.5	0.31	0.47	50.4	0.18	0.37	106	0.34	0.47	36.2

384 The prediction errors are relatively lower for the elastic constants C_{11} and C_{33} compared
385 to those for C_{13} . This can be explained by the high degree of measurement uncertainties in
386 C_{13} where the standard deviations are usually expected to be between 30% and 50% (Jones
387 and Wang 1981; Domnesteau, McCann and Sothcott 2002; Jakobsen and Johansen 2000).
388 Additionally, Sayers (2013a) studied the anisotropic response of shales and concluded that the
389 value of C_{13} can be affected by features such as the presence of microcracks in the sample,
390 which is ignored in our model. Considering the complexity of shale microstructure in addition
391 to the high standard deviations which are usually observed when measuring shale properties,

392 we conclude that the homogenisation methods can provide valuable mechanical results simply
393 and inexpensively, using just quantitative mineralogical descriptions of shales.

394 The data in Table 7 show that the anisotropy was captured very well for all the data sets.
395 However, it is obvious that the absolute predicted elastic constants are not satisfactory for the
396 case of Woodford shales in comparison with the results obtained for Kimmeridge and Jurassic
397 shales. As the homogenisation overestimates the elastic modulus, this could be due to the lack
398 of information on the confining pressures used in the Woodford data sets. This is a critical
399 parameter in the UPV test results as it can reduce the effect of microcracks, which are not con-
400 sidered in the modelling. For example, elevation in confining pressure from 5 MPa to 80 MPa
401 increases C_{11} by 40% in Jurassic shale (Hornby 1998). The TOC contents of these samples
402 were not provided in the reference which could also have significantly reduced the elastic re-
403 sponse. Moreover, it is also of interest to compare these results with previous micro-mechanical
404 modelling of the same data sets. Jakobsen et al. (2003) attempted to predict the Jurassic shale
405 elastic response. Several strategies were tried and the best results they could achieve were close
406 to the measured properties at a confining pressure of 20 MPa. Vasin et al. (2013) started with
407 a single clay particle to build up a shale model for Kimmeridge shale. They could not manage
408 to reproduce the elastic response using the shale characterization obtained experimentally. By
409 increasing the porosity to more than 10% with a specific aspect ratio, a good agreement was
410 achieved with the predicted results and the measured elastic constant at a confining pressure
411 of 80 MPa. It should be emphasised that the predicted data here are obtained solely using the
412 shale characterisation presented in the literature (Hornby 1998; Sierra et al. 2010), without any
413 further calibration.

414 **5.3 Indentation data sets**

415 **5.3.1 Indentation test**

416 Indentation tests generate mechanical properties of materials from their surface response. In
417 this test, an indenter with known mechanical properties is pushed into a material surface with
418 unknown properties. The continuous loading and unloading curves versus displacement are
419 plotted as depicted in Figure 8, and two material properties can be defined as follows:

$$H = \frac{F_{max}}{A_c} \quad (7)$$

$$M = \frac{\sqrt{\pi}}{2} \frac{S}{\sqrt{A_c}} \quad \text{with} \quad S = \left(\frac{dF}{dh} \right)_{h=h_{max}} \quad (8)$$

420 where H is defined as the indentation hardness, M is the indentation modulus, F_{max} is the
421 maximum applied force on the indenter, h_{max} is the maximum penetration depth, A_c is the
422 projected contact area on the sample, and S is the stiffness of the unloading curve at h_{max} (see
423 Figure 8).

424 Indentation hardness is related to the elastic-plastic response of the material; however, it
425 cannot be directly related to the conventional plastic parameters such as the angle of friction
426 and cohesion. Therefore, this mechanical property is mainly derived for comparison of different

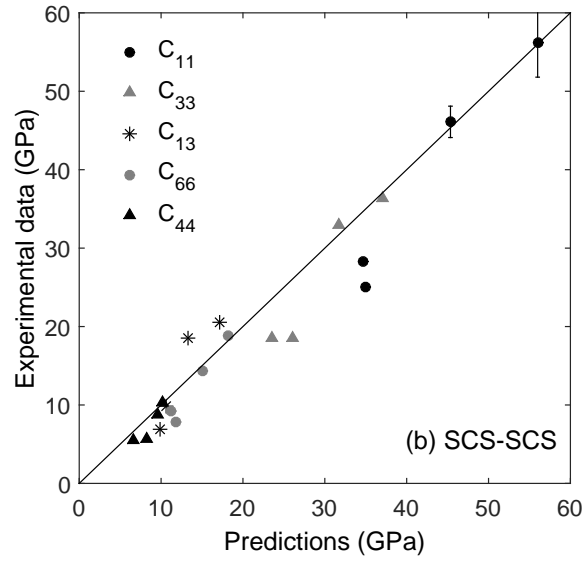
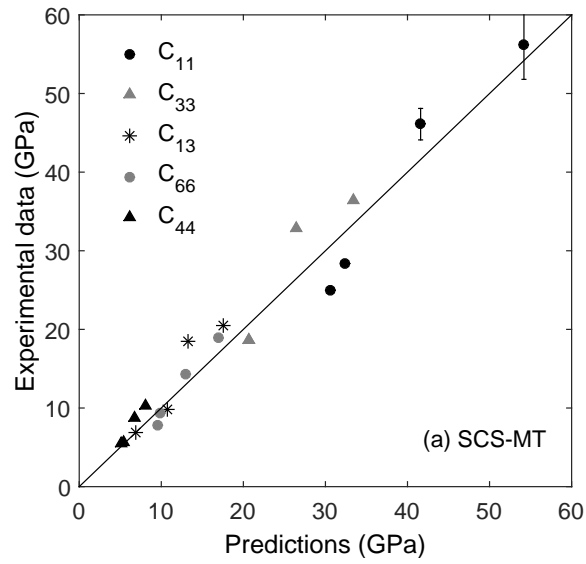


Figure 7: Summary of the experimental and predicted results for the UPV data sets shale samples using (a) SCS-SCS and (b) SCS-MT.

427 material responses. The indentation modulus, on the other hand, can be analytically related
 428 to the elastic constants of the material. For isotropic (equation 9) and transversely isotropic
 429 (equations 10 and 11) materials, it can be written as (Delafargue and Ulm 2004):

$$M = \frac{E}{1 - \nu^2} = \frac{C_{11}^2 - C_{12}^2}{C_{11}} \quad (9)$$

$$M_3 = 2\sqrt{\frac{C_{11}C_{33} - C_{13}^2}{C_{11}} \left(\frac{1}{C_{44}} + \frac{2}{\sqrt{C_{11}C_{33} + C_{13}}} \right)^{-1}} \quad (10)$$

$$M_2 = \sqrt{\frac{C_{22}^2 - C_{12}^2}{C_{11}}} \sqrt{\frac{C_{11}}{C_{33}}} M_3 \quad (11)$$

430 where M_3 is the indentation modulus when the indenter is perpendicular to bedding direction
 431 whereas M_1 is the indentation modulus when the indenter is parallel to bedding direction.

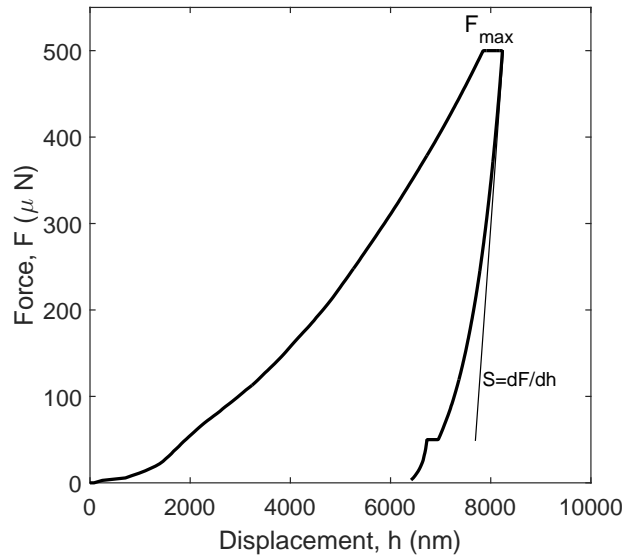


Figure 8: Loading-unloading curve versus displacement for a single indentation test on a shale thin section.

432 5.3.2 Petrological characterisation and sample mechanical properties

433 The Toarcian shales of the Paris Basin are the lateral equivalent of the Northern European Posi-
 434 donia Shale, consisting of a sequence of marine shales deposited in the Tethys Ocean during
 435 the Early Jurassic. The Toarcian shales are rich in organic material and have shale oil poten-
 436 tial (Jarvie 2012). Our samples come from the Couy-1 well which was drilled in 1986-1987.
 437 Toarcian shales are located between 210 m and 355 m (Pradier and Gauthier 1987).

438 Core samples of the Toarcian shales were selected from different depths based on the quality
 439 of the samples. QEMSCAN analysis was used to determine the mineralogy of the selected
 440 samples. QEMSCAN is an automated mineralogy method that combines electron microscopy

441 with energy dispersive spectroscopy for quantitative mineralogical analysis of rock sample.
 442 Based on the mineralogical data, four samples were selected for indentation measurements to
 443 determine the mechanical properties. Figure 9 shows digital mineralogical image generated
 444 by QEMSCAN analysis. Table 8 provides information about the total organic carbon, T_{max}
 445 index and mineralogical descriptions for the samples used in indentation tests. The following
 446 empirical relationship has been used to convert the TOC in weight percent to kerogen in volume
 447 percent (Vernik and Nur 1992; Carcione 2000):

$$K_r = \frac{TOC\rho_b}{0.75\rho_k} \quad (12)$$

448 where ρ_b is the bulk density of the sample, ρ_k is the kerogen density and K_r is the volumetric
 449 kerogen content. The values of T_{max} are less than 435 indicating that the shale samples are
 450 immature; therefore, a value of 1.25 g/cm³ was selected for the kerogen density (Okiongbo,
 451 Aplin and Larter 2005).

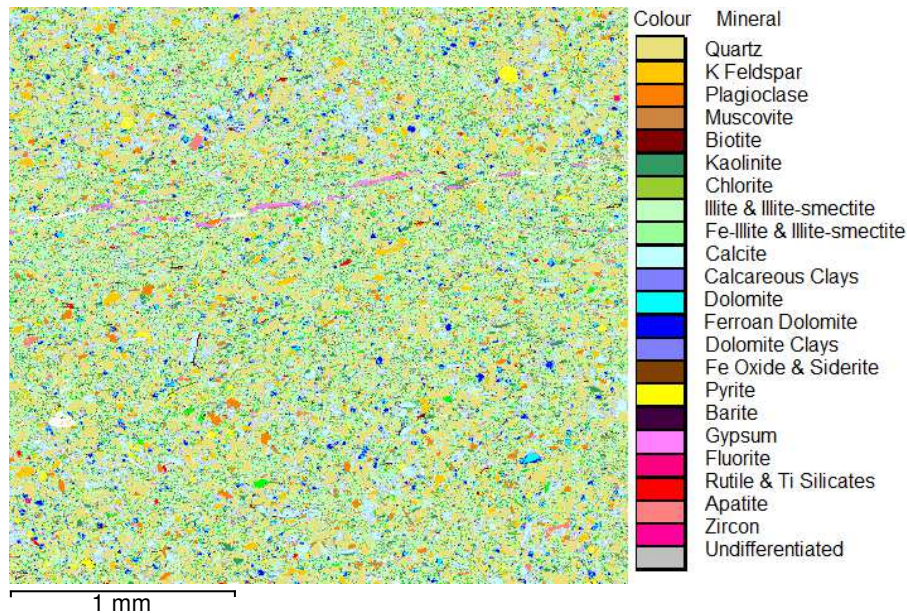


Figure 9: QEMSCAN image based on combination of SEM and EDS digital images.

452 For each shale sample two surfaces, one parallel and one perpendicular to bedding, were pre-
 453 pared and polished in order to provide relatively smooth area as for the PeakForce QNM[®] tests.
 454 Tests were performed using the Berkovich indenter along with a force-controlled condition with
 455 a maximum value of 400 mN set for all experiments. This maximum possible load was applied
 456 in order to create the maximum possible contact area and to obtain the best surface response of
 457 the whole shale composite. This force value generated indentation depths from 3.5 μm to 6.5
 458 μm , depending on the sample stiffness.

459 Due to the complex nature of shale, even at the scale of a few microns, a large number of
 460 indents must be conducted in order to obtain a robust statistical description of the mechanical
 461 response. Here, an average, around 80 indentations were conducted on each surface to char-
 462 acterise its mechanical response. It should be noted that the indentation data usually contains
 463 some out-of-range values which might be caused by the indenter mainly touching a large stiff

Table 8: Rock-Eval and volumetric mineralogical data for the indentation test shale samples.

Sample No.	2	6	8	10
Quartz	29.3	6.5	9.3	25.6
Calcite	0.8	7.4	9.6	5.8
Pyrite	0.3	1.1	6.1	2.7
Feldspar	3.6	0.2	0.6	2.6
Dolomite	1.5	2.7	1.6	1.1
Total silt inclusions	35.4	17.9	27.1	37.9
Kerogen	3.2	5.6	19.5	3.2
Porous Clay	61.3	87.68	53.4	58.9
T_{max}	432	430	419	432
TOC (Weight %)	1.1	2.0	7.5	1.1
Bulk density (g/cm ³)	2.65	2.67	2.45	2.66
Depth (m)	224.9	340	347.5	202.5

464 grain or a large pore space, generating very high or very low penetration depths, respectively.
 465 A judgment is hence required to filter the out-of-range data and to eliminate their effects on the
 466 calculation of mean and standard deviation of shale material properties (Table 9).

467 In order to better understand the source of anisotropy in these samples the anisotropy ratio
 468 (M_1/M_3) is plotted versus kerogen volume fraction in Figure 10. It can be observed that an
 469 increase in kerogen does not necessarily translate into increased anisotropy but reduces both
 470 indentation moduli significantly. This result contrasts with the correlation between anisotropy
 471 and the kerogen volume fraction suggested by Vernik and Nur (1992). However, observations
 472 from experiments reported in Vernik and Landis (1996) and Kumar (2012) show that the cor-
 473 relation between kerogen volume fraction and Thomsen's anisotropic parameter ε is relatively
 474 weak. In fact, the reported data are scattered, particularly on immature samples (Vernik and
 475 Nur 1992), which further reveals the difficulties involved in the determination of the main pa-
 476 rameters affecting shale anisotropy.

Table 9: Indentation moduli (GPa).

Sample Sample No.	M_1 (GPa)		M_3 (GPa)		Anisotropy ratio M_1/M_3
	Mean	SD	Mean	SD	
2	30.3	7.7	17.2	7.3	1.76
6	27.4	2.7	17	2.1	1.61
8	20.6	2.8	12.6	2.5	1.63
10	28.5	7.6	-	-	-

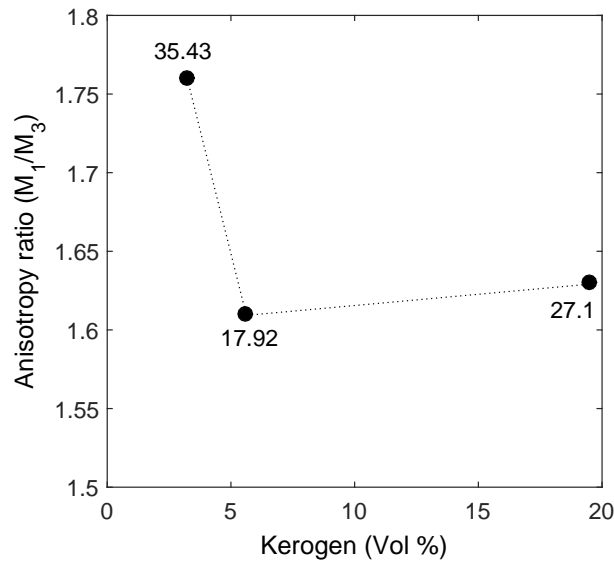


Figure 10: Anisotropy versus kerogen volume fraction (data label is the volume fraction of silt inclusions).

477 5.3.3 Homogenisation of organic-rich shales

478 In order to calculate the indentation moduli from the homogenisation technique, porosity and
 479 organic matter content should also be taken into account, in addition to the mineralogical data
 480 provided in Table 8. Here, an estimation of the porosity is required as this parameter was not
 481 measured. In addition, identifying the material properties of organic matter and its role on the
 482 overall mechanical behaviour of the shale composite is also important.

483 Due to the fact that all the samples have been retrieved from similar depths (see Table 8),
 484 it is assumed that the clay packing density, η , is the same in all samples. The clay packing
 485 density relates to the compaction state of clay particles and can be defined as: $\eta = 1 - \phi_{clay}$.
 486 This value can be back-calculated from one data set by equalising the experimental value to the
 487 predicted one. The obtained value is then used as the ‘reference parameter’ for the rest of the
 488 experimental data. In addition, as the sample had been exposed to room-temperature for a long
 489 time before the test, the shale will be considered as dry, with no fluid within the pore spaces.

490 An assumption in the homogenisation formulation is that the matrix is considered as a con-
 491 tinuous phase and the inclusions are isolated and fully surrounded by the matrix phase. SEM
 492 observations (see Figure 3) suggest that the organic matter is a semi-continuous phase mixed
 493 with the porous clay. We therefore assume that the organic matter can be considered to be
 494 part of the shale matrix so that its contribution is taken into account, along with that of the
 495 porosity, in the first level of homogenisation. Previous approaches include considering organic
 496 matter as the background phase in shale (Vernik and Landis 1996, Bayuk et al. 2008; Sayers
 497 2013b), combining kerogen and solid clay as the elementary building block of the shale matrix,
 498 or adding kerogen as inclusions (Guo et al. 2014).

499 Based on the observation that kerogen in the tested samples does not increase the anisotropy
 500 ratio, it is assumed here that kerogen is mixed with a porous clay having the same packing

501 density in all the samples. The combination of these phases through the use of SCS enables us to
502 reproduce a system of semi-continuous random pore and kerogen networks with no preferential
503 orientation. This approach is consistent with the experimental observation (Figure 10) in which
504 anisotropy is slightly reduced by an increase in kerogen. The mechanical properties of kerogen
505 are an important and controversial factor in the prediction of the overall mechanical response
506 for organic-rich shale. However, as discussed in Section 3, there is a discrepancy between
507 the reported elastic properties of kerogen in the literature. In Section 4, the nanoscale direct
508 mechanical measurements were conducted on an immature shale sample which provided a mean
509 value of 6 GPa for kerogen assuming that the Poisson's ratio is 0.3. As the current samples are
510 also immature, this value will be adopted for the micromechanical modelling.

511 Based on the predicted results in Section 5.2, the SCS homogenisation strategy was also
512 considered at the second level. The clay packing density was calibrated to be approximately
513 0.75 based on the indentation modulus parallel to the bedding direction (M_1) for sample No. 2.
514 The same packing density was adopted for the remaining samples. Figure 11 summarizes the
515 experimental data versus the predicted values for indentation moduli. Table 10 also provides
516 these values along with their relative errors.

517 Considering the standard deviations in the indentation data, which create a range for the
518 indentation moduli, it can be seen that almost all the predicted moduli are within these ranges.
519 The model shows very good predictions of the effect of changing the kerogen and inclusion vol-
520 ume fractions purely based on mineralogical composition. However, in two cases of samples
521 No. 2 and No. 8, the experimental data show a higher anisotropy ratio (M_1/M_3) than the pre-
522 dictions. This could be attributed to the simplifications which assume spherical silt inclusions
523 and pores/kerogen distributions with no preferential orientation. In addition, the presence of mi-
524 crofractures could significantly contribute to the higher anisotropy of the experimental results
525 (Sayers 2013a). Kanitpanyacharoen et al. (2010) and Vasin et al. (2013) have determined some
526 of the textural effects by quantifying orientation distributions and shapes of the minerals in dif-
527 ferent shale samples. An advanced micro-mechanical modelling approach used in these studies,
528 accounting for experimental data, did not result in satisfactory predictions in terms of P-wave
529 velocities and anisotropy. They concluded that the differences in model and experimental re-
530 sults could be attributed to the anisotropy and weaknesses induced by oriented pore structures,
531 microfractures and kerogen. Although these effects can easily be introduced into the model
532 by considering an elliptical shape for silt inclusions, pores and kerogen, it is very difficult to
533 quantify the effects by direct experimental measurements. Bayuk et al. (2008) found that when
534 these micro-structural features are unknown, considering different combinations of them in the
535 modelling can produce similar anisotropy. This is one of the drawbacks of micro-mechanical
536 modelling and also one of the reasons why a range of modelling strategies has been adopted for
537 shale. In fact, it is not reasonable to add more complexity to the modelling while the input pa-
538 rameters are not quantitatively known. The idea of using a set of TI parameters for solid clay as
539 the main source of anisotropy is a simplified yet reasonably accurate approximation for a more
540 complex shale structure. A possible solution could be to combine micro-mechanical modelling
541 with fast and efficient indentation testing on shale cuttings, which cannot solely characterise full
542 TI elastic constants of shales, in order to identify some of the potential sources of anisotropy
543 and also calibrate the micro-structural features.

Table 10: Predicted results (Pred.) versus experimental measurements (Exp.).

Sample No.	Clay packing density	Exp. M_1 (GPa)	Exp. M_3 (GPa)	Exp. M_1/M_3 -	Pred. M_1 (GPa)	Pred. M_3 (GPa)	Pred. (M_1/M_3) -	Error (%)	Error (%)
2	0.75	30.3	17.2	1.76	30.3	21.6	1.4	0.0	25
6	0.75	27.4	17	1.61	26.5	17.1	1.55	3.5	0.5
8	0.75	20.6	12.6	1.63	18.8	13.9	1.33	9	11.9
10	0.75	28.5	-	-	30.6	22.7	-	7.3	-

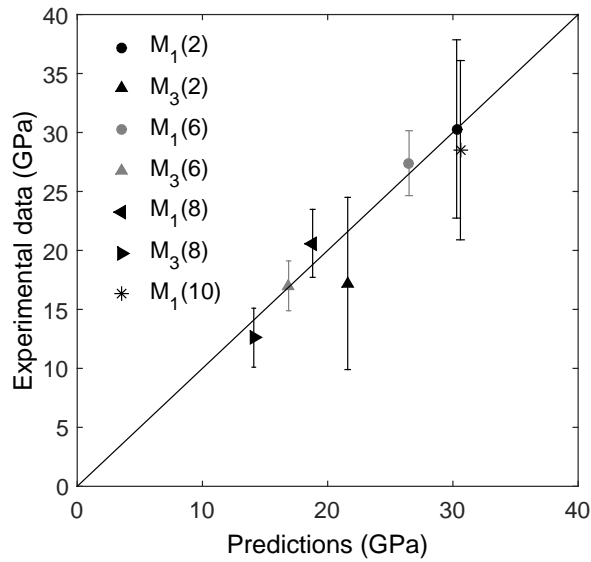


Figure 11: The experimental and predicted values for indentation moduli (vertical bars represent the standard deviations for the experimental data).

6 Conclusions

545

546

547

548

549

550

551

552

553

554

555

556

557

558

559

560

561

562

563

564

565

566

567

568

569

570

571

572

573

574

575

576

We have studied the capabilities of a range of multi-scale homogenisation techniques to model and predict the elastic response of shales. The shales were assumed to be a composite formed by a matrix containing solid clay, kerogen and pores. Solid mineral grains/inclusions were randomly distributed within the matrix. Consequently, two levels of homogenisation were required involving the SCS method at the first level to upscale the shale matrix and, at the second level, the capabilities of both MT and SCS in homogenising the matrix-inclusion morphology.

Resulting Young's modulus maps using the AFM-based PeakForce QNM[®] mechanical characterisation mode on two sections of immature, organic-rich shale, showed an isotropic response for quartz grains. The porous clay, in contrast, showed highly anisotropic behaviour with almost the same anisotropy ratio as measured at the macroscale. Organic matter is seen to be a semi-continuous phase within the porous clay matrix, with a measured Young's modulus of 6 GPa.

Results from the homogenization method were evaluated against the limited geomechanical datasets available in the literature. Considering the multiscale complexity of shales and also the high standard deviations usually obtained in mechanical experiments on shale samples, the values estimated by the homogenisation method, which are based solely on mineralogical descriptions, provide valuable predictions of the mechanical response. Additionally, comparing SCS and MT for the second level of homogenisation, it was concluded that SCS produced a slightly better prediction of elastic response with a very good estimate of anisotropy.

Finally, to generate more data for organic-rich shales easily and inexpensively, advanced indentation tests were implemented. Based on the observations in the nanoscale mechanical maps, organic matter was taken into account in the first level of homogenization with the elastic modulus being measured by nano-mechanical mapping. A comparison between the predicted indentation moduli and the experimental values confirms the capability of the multi-scale homogenization method to predict the effect of kerogen on the elastic response of shales, provided that this phase is suitably accounted for. However, micro-structural features such as grain shape or pore aspect ratio, which cannot be measured directly, need to be calibrated in order to further adjust the predicted anisotropy. This calibration can be performed with indentation data sets which can be obtained from shale cuttings. Generally, it can be concluded that the homogenization technique can be effectively used as an auxiliary approach to conventional rock mechanics tests to estimate the elastic response of shale rocks using petrological and mechanical properties of shale cuttings.

577

Acknowledgements

578

579

580

581

582

The authors would like to acknowledge the collaboration of the BRGM (the French geological survey) and SGS Horizon B.V. by providing shale samples characterisation and the experimental indentation data. The first author greatly acknowledges discussions with Mr. Leon Bowen on sample preparation, SEM and EDS analyses. We also thank Dr. Richard Thompson for providing access to the AFM facilities at Durham University.

583 Rerefences

- 584 Amirmajdi O.M., Ashyer-Soltani R., Clode M.P., Mannan S.H., Wang Y., Cabruja E. and Pel-
585 legrini G. 2009. Cross-section preparation for solder joints and MEMS device using argon ion
586 beam milling. *IEEE Transactions on electronics packaging manufacturing* **32**(4), 265-271.
- 587 Antonangeli D., Krish M., Fiquet G., Badro J., Farber D.L., Bossak A. and Merkel S. 2005.
588 Aggregate and single-crystalline elasticity of hcp cobalt at high pressure. *Physical Review B*
589 **72**, 134303.
- 590 Aplin A.C. and Macquaker J.H.S. 2011. Mudstone diversity: origin and implications for source,
591 seal and reservoir properties in petroleum systems. *The American Association of Petroleum*
592 *Geologists (AAPG) Bulletin* **95**(12), 2031-2059.
- 593 Bass J.D. 1995. Elasticity of minerals, glasses, and melts. In: *Minerals Physics & Crystallog-*
594 *raphy: A handbook of physical constants* (ed. T.J. Ahrens), pp. 45-63. *AGU Reference Shelf*.
595 ISBN 9780875908526.
- 596 Bayuk I.O., Ammerman M. and Chesnokov E.M. 2008. Upscaling of elastic properties of
597 anisotropic sedimentary rocks. *Geophysical Journal International* **172**, 842-860.
- 598 Bobko C. and Ulm F.J. 2008. The nano-mechanical morphology of shale. *Mechanics of Mate-*
599 *rials* **40**, 318-337.
- 600 Bruker's Application Note #141. Toward quantitative nanomechanical measurements on live
601 cells with PeakForce QNM. <https://www.bruker.com/products>.
- 602 Bruker's Application Note #128. Quantitative mechanical property mapping at the nanoscale
603 with PeakForce QNM. <https://www.bruker.com/products>.
- 604 Carcione J.M. 2000. A model for seismic velocity and attenuation in petroleum source rocks.
605 *Geophysics* **65**(4), 1080-1092
- 606 Chalmers G.R., Bustin R.M. and Power I.M. 2012. Characterization of gas shale pore systems
607 by porosimetry, pycnometry, surface area, and field emission scanning electron microscopy/transmission
608 electron microscopy image analyses: Examples from the Barnett, Woodford, Haynesville, Mar-
609 cellus and Doig units. *The American Association of Petroleum Geologists (AAPG)* **96**(6), 1099-
610 1119.
- 611 Delafargue A. and Ulm F.J. 2004. Explicit approximations of the indentation modulus of elas-
612 tically orthotropic solids for conical indenters. *International Journal of Solids and Structures*
613 **41**, 7351-7360.
- 614 Domnesteau P., McCann C. and Sothcott J. 2002. Velocity anisotropy and attenuation of shale
615 in under- and over pressured conditions. *Geophysical Prospecting* **50**, 487-503.
- 616 Draege A., Jakobsen M. and Johansen T.A. 2006. Rock physics modelling of shale diagenesis.
617 *Petroleum Geoscience* **12**, 49-57.
- 618 Eliyahua M., Emmanuel S., Day-Stirrat R.J. and Macaulay C.I. 2015. Mechanical properties
619 of organic matter in shales mapped at the nanometer scale. *Marine and Petroleum Geology* **59**,

620 294-304.

621 Fritsch A. and Hellmich C. 2007. Universal microstructural patterns in cortical and trabecular,
622 extracellular and extravascular bone materials: Micromechanics-based prediction of anisotropic
623 elasticity. *Journal of Theoretical Biology* **244**, 597-620.

624 Goodarzi M., Rouainia M. and Aplin A.C. 2016. Evaluation of multi-scale homogenisation
625 methods for the case of clayey rock elastic properties using numerical simulation. *Computa-
626 tional Geosciences* 1-14, doi:10.1007/s10596-016-9579-y

627 Guo Z.Q., Li X.Y. and Liu C. 2014. Anisotropy parameters estimate and rock physics analysis
628 for the Barnett Shale. *Journal of Geophysics and Engineering* **11**, 065006.

629 Heyliger P., Ledbetter H. and Kim S. 2003. Elastic constants of natural quartz. *The Journal of
630 the Acoustical Society of America* **114**, 644-650.

631 Hill R. 1965. A self-consistent mechanics of composite materials. *Journal of Mechanics and
632 Physics of Solids* **13**, 213-222.

633 Hornby B.E., Schwartz L. and Hudson J. 1994. Anisotropic effective medium modelling of the
634 elastic properties of shales. *Geophysics* **59**, 1570-83.

635 Hornby B.E. 1998. Experimental laboratory determination of the dynamic elastic properties of
636 wet, drained shales. *Journal of Geophysical Research* **103**(B12), 29945-29964.

637 Jakobsen M. and Johansen T.A. 2000. Anisotropic approximations for mudrocks: A seismic
638 laboratory study. *Geophysics* **65**(6), 1711-1725.

639 Jakobsen M., Hudson J.A. and Johansen T.A. 2003. T-matrix approach to shale acoustics.
640 *Geophysical Journal International* **154**, 533-558

641 Jarvie D.M. 2012. Shale resource systems for oil and gas: Part 2 Shale-oil resource systems.
642 In: *Shale reservoirs Giant resources for the 21st century* (ed. J.A. Breyer), pp. 89-119. AAPG
643 Memoir Volume **97**. ISBN 978-1-62981-011-9.

644 Jones L.E.A. and Wang H.F. 1981. Ultrasonic velocities in Cretaceous shales from the Williston
645 basin. *Geophysics* **46**(3), 288-297.

646 Kanitpanyacharoen W., Wenk H.R., Kets F., Lehr C. and Wirth R. 2011. Texture and anisotropy
647 analysis of Qusaiba shales. *Geophysical Prospecting* **59**, 536-556.

648 Klusemann B., Bohm H.J. and Svendsen B. 2012. Homogenisation methods for multi-phase
649 elastic composites with non-elliptical reinforcements: Comparisons and benchmarks. *European
650 Journal of Mechanics - A/Solids* **34**, 21-37.

651 Kumar V., Sondergeld C.H. and Rai C.H. 2012. Nano to macro mechanical characterization
652 of shale. SPE Annual Technical Conference and Exhibition, San Antonio, Texas, USA. SPE
653 159804.

654 Kumar V. 2012. Geomechanical Characterization of Shale Using Nano-indentation. MSc dis-
655 sertation, University of Oklahoma.

656 Laws N. 1977. The determination of stress and strain concentrations at an ellipsoidal inclusion

657 in an anisotropic material. *Journal of Elasticity* **7**(1), 91-97.

658 Mavko G., Mukerji T. and Dvorkin J. 2009. The Rock Physics Handbook. Cambridge Univer-
659 sity Press. ISBN 9780521861366.

660 Mori T. and Tanaka K. 1973. Average stress in matrix and average elastic energy of materials
661 with misfitting inclusions. *Acta Metallurgica* **21**, 571-574.

662 Mortazavi B., Baniassadi M., Bardon J. and Ahzi S. 2013. Modelling of two-phase random
663 composite materials by finite element, Mori-Tanaka and strong contrast methods. *Composites:
664 Part B* **45**, 1117-1125.

665 Okiongbo K.S., Aplin A.C. and Larter S.R. 2005. Changes in Type II Kerogen Density as a
666 Function of Maturity: Evidence from the Kimmeridge Clay Formation. *Energy & Fuels* **19**,
667 2495-2499.

668 Ortega J.A., Ulm F.J. and Abousleiman Y. 2007. The effect of the nanogranular nature of shale
669 on their poroelastic behaviour. *Acta Geotechnica* **2**, 155-182.

670 Ortega J.A., Ulm F.J. and Abousleiman Y. 2010. The effect of particle shape and grain-scale
671 properties of shale: A micromechanics approach. *International Journal of Numerical and Ana-
672 lytical Method in Geomechanics* **34**, 1124-1156.

673 Peng S., Yang J., Xiao X., Loucks B., Ruppel S. and Zhang T. 2015. An integrated method
674 for upscaling pore-network characterization and permeability estimation: example from the
675 Mississippian Barnett shale. *Transport in Porous Media* **109**, 359-376.

676 Pradier B. and Gauthier B. 1987. Etude préliminaire de la matière organique sédimentaire. In:
677 *Géologie profonde de la France, forage scientifique de Sancerre-Couy* (ed. C. Lorenz), pp.
678 103-108. Documents n°135 du Bureau de Recherches Géologiques et Minières (BRGM). in
679 French

680 Qin X., Han D. and Zhao L. 2014. Rock physics modeling of organic-rich shales with different
681 maturity levels. *SEG Technical Program Expanded Abstracts*, 2952-2957.

682 Sayers C.M. 1994. The elastic anisotropy of shales. *Journal of Geophysical Research* **99**(B1),
683 767-774.

684 Sayers C.M. 2013a. The effect of anisotropy on the Young's moduli and Poisson's ratios of
685 shales. *Geophysical Prospecting* **61**, 416-426.

686 Sayers C.M. 2013b. The effect of kerogen on the elastic anisotropy of organic-rich shales.
687 *Geophysics* **78**, (2), D65-D74.

688 Sierra R., Tran M.H., Abousleiman Y.N. and Slatt R.M. 2010. Woodford Shale Mechanical
689 Properties and the Impacts of Lithofacies. The 44th US Rock Mechanics Symposium and 5th
690 US-Canada Rock Mechanics Symposium. Salt Lake City ARMA-10-461

691 Trtik P., Kaufmann J. and Volz U. 2012. On the use of peak-force tapping atomic force mi-
692 croscopy for quantification of the local elastic modulus in hardened cement paste. *Cement and
693 Concrete Research* **42**, 215-221.

694 Ulm F.J. and Abousleiman Y. 2006. The nanogranular nature of shale. *Acta Geotechnica* **1**,

695 77-88.

696 Vasin R.N., Wenk H.R., Kanitpanyacharoen W., Matthies S. and Wirth R. 2013. Elastic anisotropy
697 modeling of Kimmeridge shale. *Journal of Geophysical Research: Solid Earth* **118**, 3931-3956.

698 Vernik L. and Nur A. 1992. Ultrasonic velocity and anisotropy of hydrocarbon source rocks.
699 *Geophysics* **57**, 727-735.

700 Vernik L. and Landis C. 1996. Elastic anisotropy of source rocks: Implication for HC generation
701 and primary migration. *AAPG Bulletin* **80**, 531-544.

702 Vernik L. and Milovac J. 2011. Rock physics of organic shales. *The Leading Edge* **30**, 318-323.

703 Wang Z., Wang H. and Cates M.E. 2001. Effective elastic properties of solid clays. *Geophysics*
704 **66**(2), 428-440.

705 Whitaker M.L., Liu W., Wang L. and Li B. 2010. Acoustic velocities and elastic properties of
706 Pyrite (FeS₂) to 9.6 GPa. *Journal of Earth Science* **21**, 792-800.

707 Wu X., Chapman M., Li X.Y. and Dai H. 2012. Anisotropic elastic modelling for organic shales.
708 74th EAGE Conference and Exhibition SPE EUROPE, Copenhagen, Denmark, P314

709 Yan F. and Han D. 2013. Measurement of elastic properties of kerogen. 83rd SEG Annual
710 Meeting, Houston, USA, Expanded Abstracts, 2778-2782

711 Zargari S., Prasad M., Mba K.C. and Mattson E.D. 2013. Organic maturity, elastic properties,
712 and textural characteristics of self-resourcing reservoirs. *Geophysics* **78**(4), D223-D235.

713 Zeszotarski J.C., Chromik R.R., Vinci R.P., Messmer M.C., Michels R. and Larsen J.W. 2004.
714 Imaging and mechanical property measurements of kerogen via nanoindentation. *Geochimica*
715 *et Cosmochimica Acta* **68**, 4113-4119.

716 Zhu Y., Xu S., Payne M., Martinez A., Liu E., Harris C. and Bandyopadhyay K. 2012. Improved
717 rock-physics model for shale gas reservoirs. 82nd SEG Meeting, Denver, USA, Expanded
718 Abstracts 2952-2957.

719 Zu Y., Xu S., Liu E., Payne M.A. and Terrell M.J. 2013. Predicting anisotropic source rock
720 properties from well data: U.S. Patent 2013/0013209 A1.